

Stray light correction algorithm for multichannel hyperspectral spectrographs

M. E. Feinholz,^{1,*} S. J. Flora,¹ S. W. Brown,² Y. Zong,² K. R. Lykke,² M. A. Yarbrough,¹
B. C. Johnson,² and D. K. Clark³

¹Moss Landing Marine Laboratories, 8272 Moss Landing Road, Moss Landing, California 95039, USA

²National Institute of Standards and Technology, 100 Bureau Drive, Gaithersburg, Maryland 20899, USA

³Joint NIST/USURF Program in Optical Sensor Calibration, Space Dynamics Laboratory,
1695 N. Research Park Way, Logan, Utah 84341, USA

*Corresponding author: feinholz@mml.calstate.edu

Received 9 January 2012; accepted 26 March 2012;
posted 10 April 2012 (Doc. ID 161112); published 1 June 2012

An algorithm is presented that corrects a multichannel fiber-coupled spectrograph for stray or scattered light within the system. The efficacy of the algorithm is evaluated based on a series of validation measurements of sources with different spectral distributions. This is the first application of a scattered-light correction algorithm to a multichannel hyperspectral spectrograph. The algorithm, based on characterization measurements using a tunable laser system, can be extended to correct for finite point-spread response in imaging systems. © 2012 Optical Society of America

OCIS codes: 010.0010, 110.4234, 290.2648, 140.3460, 060.2310.

1. Introduction

Multichannel spectrometers, such as multiple-fiber-input spectrographs, allow the simultaneous acquisition of spectrally resolved data sets from spatially distinct targets. They are widely distributed throughout a number of industries for applications ranging from product quality assurance to high-throughput medical diagnostics. As multichannel nonimaging systems (and imaging systems) are increasingly used in quantitative optical metrological applications, the need for a more complete understanding of the radiometric performance of the instrument intensifies.

Scattered, or stray, light (SL) within an input channel (along the spectral or dispersion direction) as well as channel-to-channel cross talk (spatial direction) arising from improperly imaged, or scattered, optical radiation within an instrument is often difficult to properly characterize and is commonly a dominant

measurement error—particularly when the spectral distribution of a source differs significantly from that of the calibration source. A one-dimensional (nonimaging, single-input) SL correction (SLC) algorithm has been developed previously for the correction of spectral SL in spectrographs [1,2] and the foundation for the two-dimensional SLC algorithm, describing the correction of spatial SL in imaging systems, has been laid [3,4].

In this work, a two-dimensional SLC algorithm is presented that accounts and corrects for SL error in a multiple-input hyperspectral spectrograph system. The algorithm is a special case of the spatial SLC algorithm for hyperspectral imaging systems [3–5]. In contrast to conventional point-spread correction algorithms that focus on sharpening up imagery—focusing on the region where the point-spread function has significant weight [6,7]—this algorithm focuses on the cumulative effects of a finite point-spread function in the region where the point-spread function has minimal weight (typically under 1%). The algorithm simultaneously corrects for

along-track (within a channel) and cross-track (channel-to-channel) SL. It has applications in improving the image contrast in high-contrast scenes, such as are commonly observed in satellite remote sensing of ocean and cloud scenes [8,9] as well as in optical medical imaging applications. The results represent the first description of a SL correction algorithm for a multichannel spectrograph system and have direct implications for correction of imaging sensors for finite point-spread response [3,4,9–11]. In form and function it is very similar to the SL correction algorithm developed by Jansson *et al.* for correcting SL errors in image scanners and digital still cameras [5,11,12]. In contrast to the previous work, the algorithm presented here does not rely on iterative solutions to the problem [1–4].

2. Stray Light Correction Algorithm

In a perfect system with monochromatic excitation, an image of the entrance slit is formed on the detector array and no light outside of this image is detected. This signal, encompassing several columns on the two-dimensional detector array or elements in a single-channel diode array system, represents the measurand of interest. The detector response to this input is the properly imaged, or in-band (IB), signal. In a real system, the imaged slit is modified by SL in the system; this scattered radiation can fall on any element in the detector array. In general, the total measured signal consists of both IB light and SL,

$$Y_{\text{meas}} = Y_{\text{IB}} + Y_{\text{SL}}. \quad (1)$$

Let n = the number of columns (or elements) in the array. The detector array elements can be arranged in a $n \times 1$ vector, with each input channel given by the superscript i ,

$$\vec{Y}_{\text{meas}}^i = \begin{bmatrix} y_{\text{meas}}^{i,1} \\ y_{\text{meas}}^{i,2} \\ \vdots \\ y_{\text{meas}}^{i,n} \end{bmatrix}, \quad \vec{Y}_{\text{IB}}^i = \begin{bmatrix} y_{\text{IB}}^{i,1} \\ y_{\text{IB}}^{i,2} \\ \vdots \\ y_{\text{IB}}^{i,n} \end{bmatrix}, \quad \text{and} \quad \vec{Y}_{\text{SL}}^i = \begin{bmatrix} y_{\text{SL}}^{i,1} \\ y_{\text{SL}}^{i,2} \\ \vdots \\ y_{\text{SL}}^{i,n} \end{bmatrix}. \quad (2)$$

Further grouping array elements according to channel, letting m = the number of input channels to the spectrograph, yields single-column vectors with dimensions $(m \times n) \times 1$:

$$\vec{Y}_{\text{meas}} = \begin{bmatrix} \vec{Y}_{\text{meas}}^1 \\ \vec{Y}_{\text{meas}}^2 \\ \vdots \\ \vec{Y}_{\text{meas}}^m \end{bmatrix}, \quad \vec{Y}_{\text{IB}} = \begin{bmatrix} \vec{Y}_{\text{IB}}^1 \\ \vec{Y}_{\text{IB}}^2 \\ \vdots \\ \vec{Y}_{\text{IB}}^m \end{bmatrix}, \quad \text{and} \quad \vec{Y}_{\text{SL}} = \begin{bmatrix} \vec{Y}_{\text{SL}}^1 \\ \vec{Y}_{\text{SL}}^2 \\ \vdots \\ \vec{Y}_{\text{SL}}^m \end{bmatrix}. \quad (3)$$

The SL signal at an element is the sum of all SL contributions falling on different elements in the array as well as a contribution from incident radiant flux not imaged onto the detector array (that is, outside the designed spectral range of the instrument). The SL signal refers to that fraction of the light properly imaged at element k in the array that is detected at element l . For each element k , there is a $1 \times (m \times n)$ array that describes the scattering into that element. Values within the IB area, that is, the value of k and neighboring elements in the array, are set to 0. Grouping these one-dimensional arrays into a two-dimensional array, the SL vector, \vec{Y}_{SL} , can be expressed as a fractional part of the in-band signal; that is,

$$\vec{Y}_{\text{SL}} = \overset{\leftrightarrow}{D} \cdot \vec{Y}_{\text{IB}} + \vec{\delta}. \quad (4)$$

The rank-two scattering tensor, $\overset{\leftrightarrow}{D}$, called the SL distribution matrix (SDM), has element magnitudes expressed as fractional contributions from the IB signal. It fully describes the SL characteristics of the system for light within the spectrograph's spectral range, that is, for light whose dominant component is properly imaged onto the array. There is an additional vector, $\vec{\delta}$, in Eq. (4) that represents the sum of the detector response to source radiant flux outside the instrument's spectral range, that is, incident flux not imaged onto the detector array. Because there is no fractional IB signal to normalize the detector response to, it cannot be quantified and corrected with the method presently described. However, this component may be negligible or can be reduced to a negligible level by using band-pass filters to block out-of-range radiation from entering the spectrograph. In the following discussion, $\vec{\delta}$ is assumed to be zero.

For each channel i , the \vec{Y}_{SL}^i column vector can be expressed as

$$Y_{\text{SL}}^i = \sum_j \overset{\leftrightarrow}{D}^{i,j} Y_{\text{IB}}^j, \quad (5)$$

where i represents the channel of interest and the summation j runs over all channels, including i . Equation (5), written explicitly, is given by

$$\vec{Y}_{\text{SL}} = \begin{bmatrix} \vec{Y}_{\text{SL}}^1 \\ \vec{Y}_{\text{SL}}^2 \\ \vdots \\ \vec{Y}_{\text{SL}}^m \end{bmatrix} = \begin{bmatrix} \sum_j \overset{\leftrightarrow}{D}^{1j} \vec{Y}_{\text{IB}}^j \\ \sum_j \overset{\leftrightarrow}{D}^{2j} \vec{Y}_{\text{IB}}^j \\ \vdots \\ \sum_j \overset{\leftrightarrow}{D}^{mj} \vec{Y}_{\text{IB}}^j \end{bmatrix} = \begin{bmatrix} \overset{\leftrightarrow}{D}^{1,1} \overset{\leftrightarrow}{D}^{1,2} \overset{\leftrightarrow}{D}^{1,3} & \overset{\leftrightarrow}{D}^{1,m} \\ \overset{\leftrightarrow}{D} & \overset{\leftrightarrow}{D} & \overset{\leftrightarrow}{D} & \dots \overset{\leftrightarrow}{D} \\ \overset{\leftrightarrow}{D}^{2,1} \overset{\leftrightarrow}{D}^{2,2} \overset{\leftrightarrow}{D}^{2,3} & \overset{\leftrightarrow}{D}^{2,m} \\ \overset{\leftrightarrow}{D} & \overset{\leftrightarrow}{D} & \overset{\leftrightarrow}{D} & \dots \overset{\leftrightarrow}{D} \\ \vdots & \vdots \\ \overset{\leftrightarrow}{D}^{m,1} \overset{\leftrightarrow}{D}^{m,2} \overset{\leftrightarrow}{D}^{m,3} & \overset{\leftrightarrow}{D}^{m,m} \\ \overset{\leftrightarrow}{D} & \overset{\leftrightarrow}{D} & \overset{\leftrightarrow}{D} & \dots \overset{\leftrightarrow}{D} \end{bmatrix} \cdot \begin{bmatrix} \vec{Y}_{\text{IB}}^1 \\ \vec{Y}_{\text{IB}}^2 \\ \vdots \\ \vec{Y}_{\text{IB}}^m \end{bmatrix}. \quad (6)$$

Each tensor $\overset{\leftrightarrow}{D}^{ij}$ is an $n \times n$ element array; there is a total of m^2 $\overset{\leftrightarrow}{D}^{ij}$ tensors. As an example, $\overset{\leftrightarrow}{D}^{1,1}$ is explicitly expressed as

$$\overset{\leftrightarrow}{D}^{1,1} = \begin{bmatrix} d_{1,1}^{1,1} & d_{1,2}^{1,1} & \dots & d_{1,j}^{1,1} & \dots & d_{1,n-1}^{1,1} & d_{1,n}^{1,1} \\ d_{2,1}^{1,1} & d_{2,2}^{1,1} & \dots & d_{2,j}^{1,1} & \dots & d_{2,n-1}^{1,1} & d_{2,n}^{1,1} \\ \dots & \dots & \dots & \dots & \dots & \dots & \dots \\ d_{x,1}^{1,1} & d_{x,2}^{1,1} & \dots & d_{x,j}^{1,1} & \dots & d_{x,n-1}^{1,1} & d_{x,n}^{1,1} \\ \dots & \dots & \dots & \dots & \dots & \dots & \dots \\ d_{n-1,1}^{1,1} & d_{n-1,2}^{1,1} & \dots & d_{n-1,j}^{1,1} & \dots & d_{n-1,n-1}^{1,1} & d_{n-1,n}^{1,1} \\ d_{n,1}^{1,1} & d_{n,2}^{1,1} & \dots & d_{n,j}^{1,1} & \dots & d_{n,n-1}^{1,1} & d_{n,n}^{1,1} \end{bmatrix}. \quad (7)$$

The diagonal tensors, $\overset{\leftrightarrow}{D}^{i,i}$, describe the scattering within a channel. Tensors $\overset{\leftrightarrow}{D}^{i,j}$, where $i \neq j$, describe the cross-track coupling from channel j into channel i . The columns in Eq. (6) correspond to scattering from channel i into the other channels. To fill the columns in each tensor, the responses of the system to monochromatic sources are recorded. Monochromatic light input into channel i giving rise to a signal at column k on the sensor array is normalized by the IB signal falling on channel i . These fractional SL values fill the k th column of all $\overset{\leftrightarrow}{D}^{i,j}$ tensors. Typically, a subset of columns is filled using measured values; intermediate column elements are filled by interpolating between measured results. In a hyperspectral system, the image of the entrance slit on the detector

array for monochromatic input flux encompasses several pixels. Assume an image on the detector array is $\pm\alpha$ elements wide. Matrix elements within $\pm\alpha$ elements along the diagonal in the along-track tensors, $\overset{\leftrightarrow}{D}^{i,i}$, are set to 0. Explicitly, matrix elements of $d_{k,l}^{i,i}$ over the range $k - \alpha < l < k + \alpha$ are set to 0.

Substituting for \vec{Y}_{SL} , Eq. (3) can be expressed as

$$\vec{Y}_{\text{meas}} = \vec{Y}_{\text{IB}} + \vec{Y}_{\text{SL}} = \vec{Y}_{\text{IB}} + \overset{\leftrightarrow}{D} \cdot \vec{Y}_{\text{IB}}. \quad (8)$$

In the final step in the algorithm, the IB signal is collapsed into a delta function; neighboring, normally nonzero IB elements are set to 0, and the integrated IB response is given along the diagonal,

$$\vec{Y}_{\text{IB}} = I \cdot \vec{Y}_{\text{IB}}, \quad (9)$$

where I is the identity matrix. \vec{Y}_{meas} can now be expressed as

$$\vec{Y}_{\text{meas}} = [I + \overset{\leftrightarrow}{D}] \cdot \vec{Y}_{\text{IB}}. \quad (10)$$

Finally, solving for \vec{Y}_{IB} ,

$$\vec{Y}_{\text{IB}} = [I + \overset{\leftrightarrow}{D}]^{-1} \cdot \vec{Y}_{\text{meas}} = \overset{\leftrightarrow}{A}^{-1} \cdot \vec{Y}_{\text{meas}},$$

$$\overset{\leftrightarrow}{A} = [I + \overset{\leftrightarrow}{D}]. \quad (11)$$

Equation (11) is a system of simultaneous linear equations with the same number of equations as unknowns; each unknown column vector \vec{Y}_{IB} can be obtained by directly solving Eq. (11) using a proper linear algebraic algorithm (e.g., the Gaussian elimination algorithm). The system of equations can also be solved using a Taylor series expansion. Because $\overset{\leftrightarrow}{D} \ll 1$, the Taylor series can be terminated after one or two terms in the series. However, in terms of simplicity and calculation speed, it is preferable to solve Eq. (9) by inverting matrix $\overset{\leftrightarrow}{A}$,

$$\vec{Y}_{\text{IB}} = \overset{\leftrightarrow}{A}^{-1} \cdot \vec{Y}_{\text{meas}} = \overset{\leftrightarrow}{C} \cdot \vec{Y}_{\text{meas}}. \quad (12)$$

where $\overset{\leftrightarrow}{C}$, the inverse of $\overset{\leftrightarrow}{A}$, is the SL correction matrix. To obtain the SL-corrected values, the measured signal is simply multiplied by $\overset{\leftrightarrow}{C}$. Development of the matrix $\overset{\leftrightarrow}{C}$ is required only once unless the imaging characteristics of the instrument change. Using Eq. (12), the SL correction becomes a single matrix multiplication operation. Note that this algorithm does not affect the resolution of the instrument: it neither sharpens nor blurs the properly imaged radiation.

3. Application to a Multichannel Spectrograph

The multichannel spectrograph system is based on a Horiba Jobin Yvon CP140 $f/2.0$ spectrograph, uses a

concave reflective grating as the dispersion element, and has an Andor CCD detector at the focal plane. (Certain commercial equipment, instruments, or materials are identified in this report in order to specify the experimental procedure adequately. Such identification is not intended to imply recommendation or endorsement by the National Institute of Standards and Technology, nor is it intended to imply that the materials or equipment identified are necessarily the best available for the purpose.) The CCD has 1024 pixels of $25\ \mu\text{m}$ in the dispersion direction, covering the spectral range from 326 nm to 965 nm, and 256 pixels along the slit height (spatial direction). The system has four 1 mm core diameter input fibers; the fibers, aligned with the entrance slit, formed spatially separated images or channels on the CCD. The response of the spectrograph system when all four input channels measure a broadband spectral source is shown in Fig. 1. The rectangular boxes outlined with black define each channel; CCD detector counts or digital numbers (DNs) are integrated over the slit direction for each channel, resulting in a single spectrum for each fiber input. Figure 2 shows the CCD response with a filtered Xe arc source input into channel 2 and no light input into the other channels. The finite responses from channels 1, 3, and 4 in the figure arise from SL; this form of SL is commonly referred to as cross-channel coupling. In Fig. 3, the signal from channels 1, 3, and 4 are shown in ratio to the signal from channel 2 for pixels 400 to 900. In this region, the cross-track coupling is on the order of 0.25% for neighboring channels 1 and 3, decreasing to 0.1% for channel 4.

An instrument's response to stray light is characterized by measuring monochromatic spectral line sources. Broadly tunable narrowband lasers in the

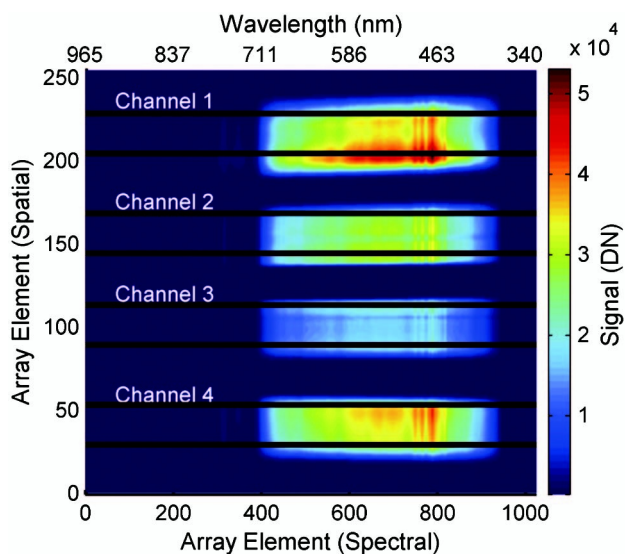


Fig. 1. Andor CCD image showing the four input channels to the spectrograph illuminated by an IR-filtered Xe arc source. The edges of each channel are denoted with solid black lines. The spectral, or dispersion, dimension and the spatial dimension are labeled in the figure.

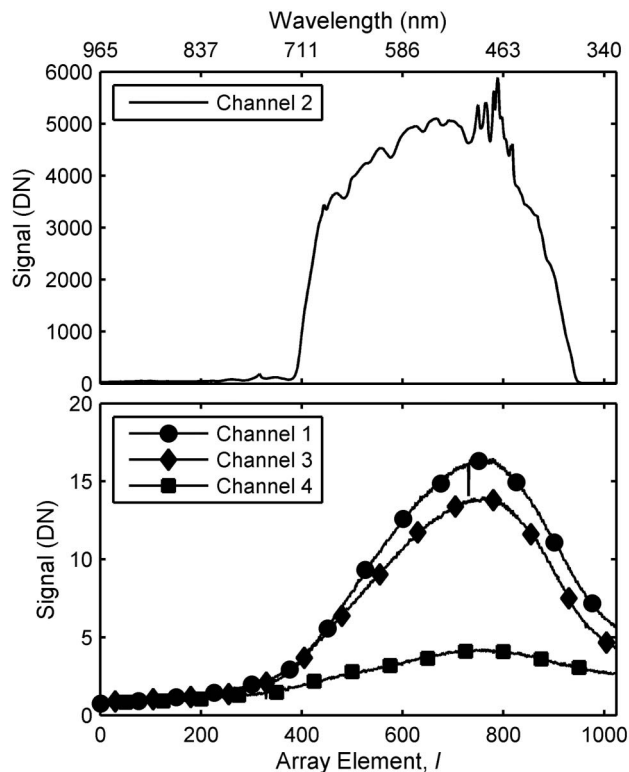


Fig. 2. (Top) Signal from channel 2 when illuminated by a Xe arc source. (Bottom) The signal from channels 1, 3, and 4, with only channel 2 illuminated by a Xe arc source.

National Institute of Standards and Technology (NIST) facility for Spectral Irradiance and Radiance Responsivity Calibrations using Uniform Sources (SIRCUS) were used to characterize the SL response of the system [13]. In this case, the spectral SL

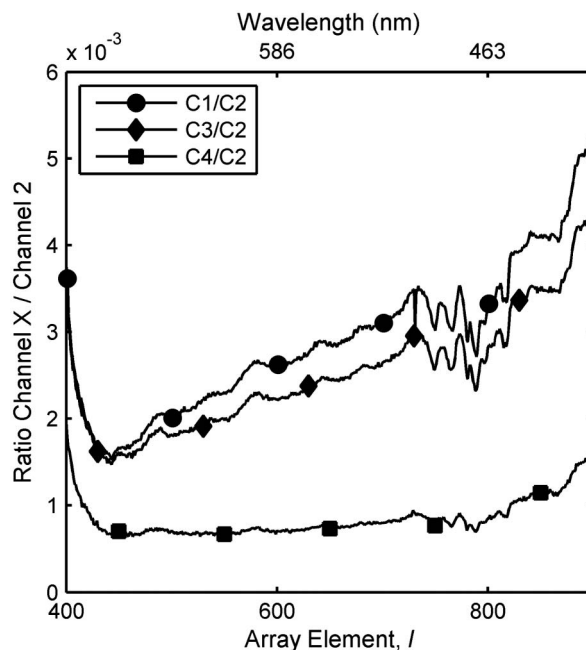


Fig. 3. Ratio of signals from channels 1, 3, and 4 to the signal from channel 2, with channel 2 illuminated by a Xe arc source.

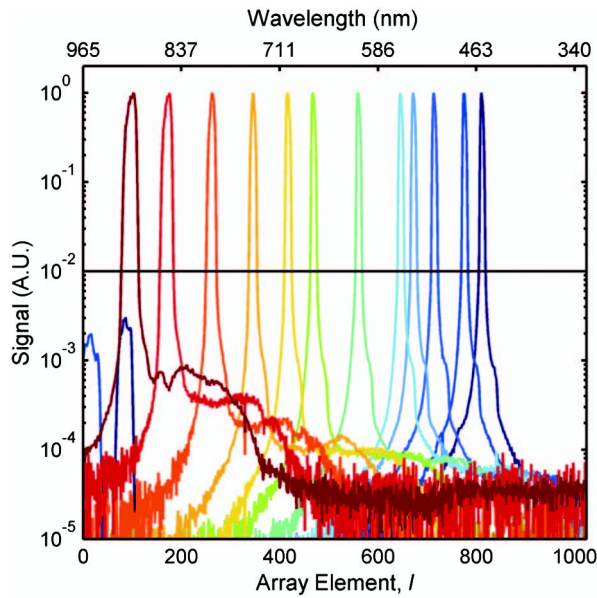


Fig. 4. Subset of the imaged laser lines used to characterize the along-track scattering from channel 2. The dark black horizontal line denotes the transition point between IB, or properly imaged, radiation and OOB, or scattered, radiation. It is set at 1% of the peak value. Note that the vertical axis is scaled in arbitrary units (A.U.).

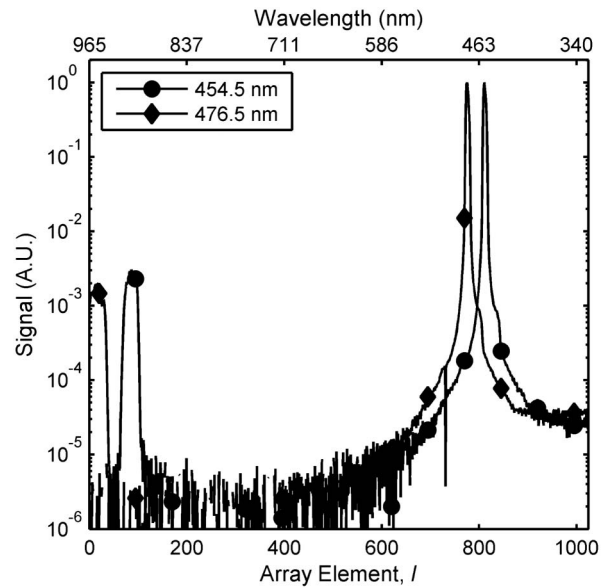


Fig. 5. Expanded image on the CCD for laser input between 450 nm and 480 nm. The peak for the laser images on the right-hand side of the graph was set to a value of 1. Note the light from second-order diffracted light falling on the CCD between 880 nm and 980 nm.

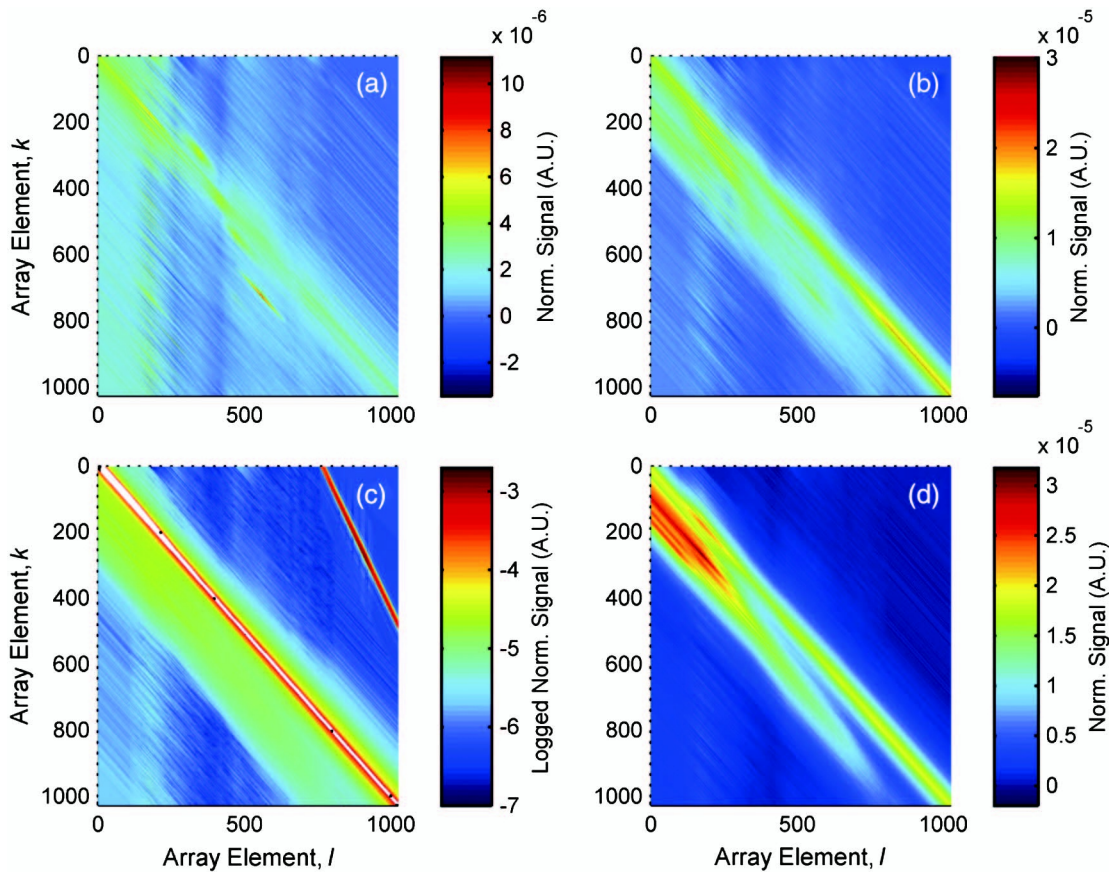


Fig. 6. Four $\overleftrightarrow{D}^{3,j}$ submatrices that describe (a) scattering from channel 1 into channel 3 ($\overleftrightarrow{D}^{3,1}$), (b) scattering from channel 2 into channel 3 ($\overleftrightarrow{D}^{3,2}$), (c) scattering within channel 3 ($\overleftrightarrow{D}^{3,3}$) and (d) scattering from channel 4 into channel 3 ($\overleftrightarrow{D}^{3,4}$). Each submatrix has 1024×1024 elements (the number of elements in the detector array).

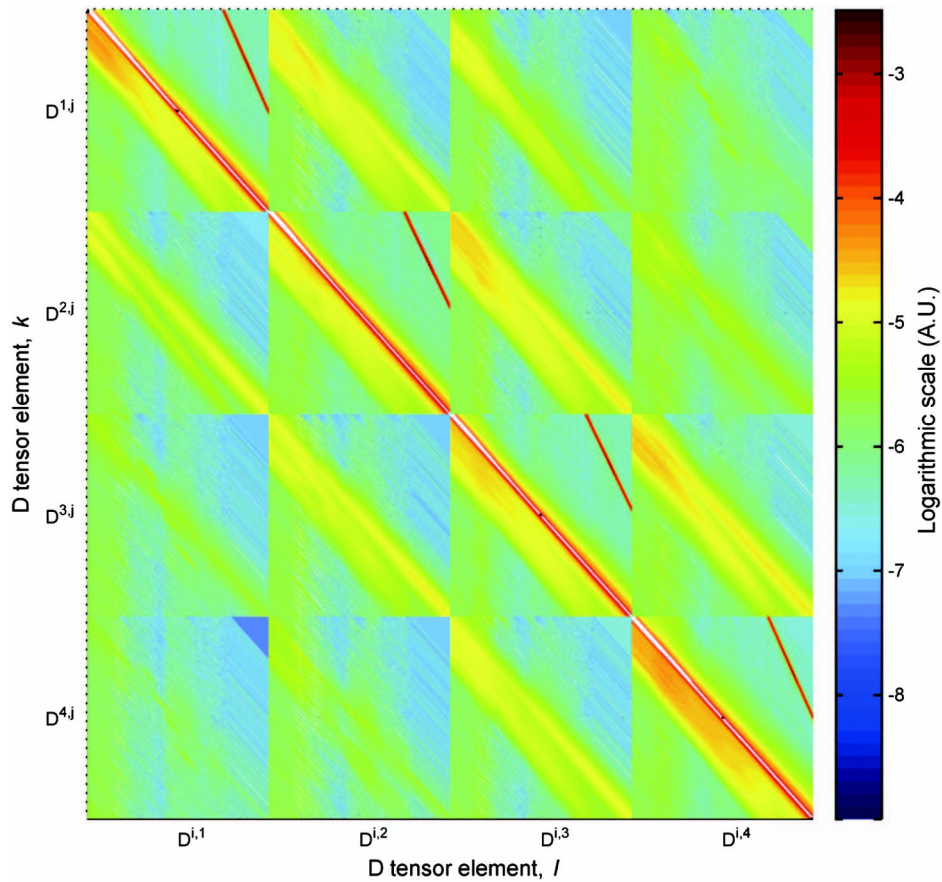


Fig. 7. Full SL distribution function matrix, \vec{D} . Note that the pixels along the diagonal (within the IB area) are 0 by definition.

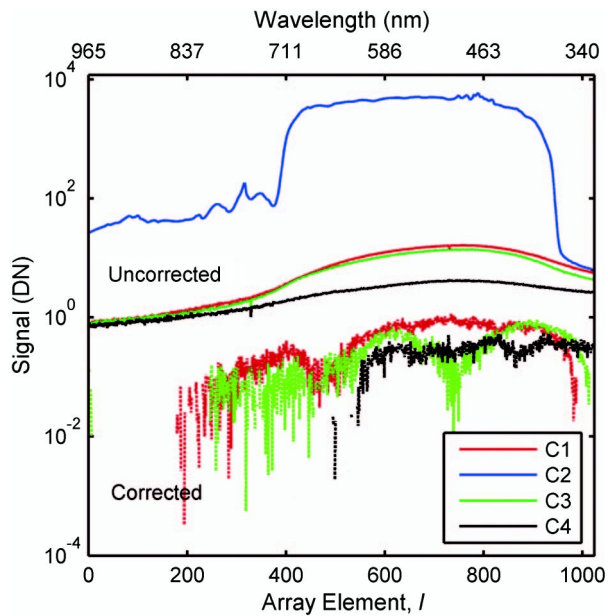


Fig. 8. Uncorrected and SL-corrected signals from the spectrograph for a single channel, channel 2, illuminated by radiation from a Xe arc lamp. Solid colored lines are uncorrected signals from all four channels; dashed colored lines are SL-corrected signals from channels 1, 3, and 4.

response can be easily separated from the desired signal: any response measured by array elements outside the instrument's bandpass arises from scattered, or improperly imaged, light. The excitation source should uniformly fill the instrument's

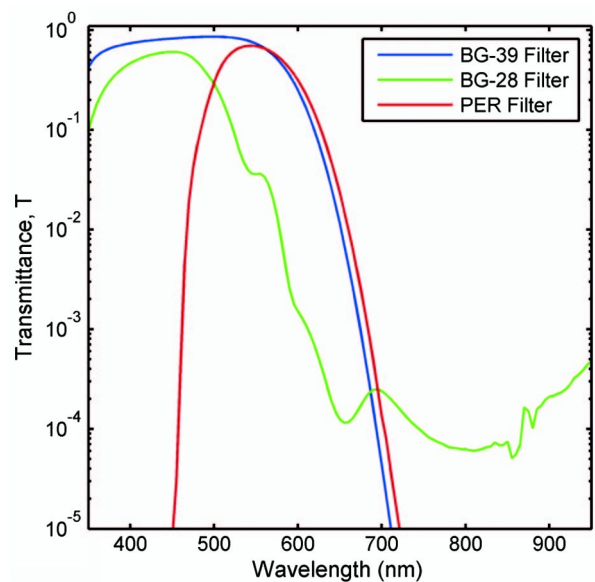


Fig. 9. Transmittance filter types used with the Xe source, a BG-39 filter, a BG-28 filter, and a PER photopic filter.

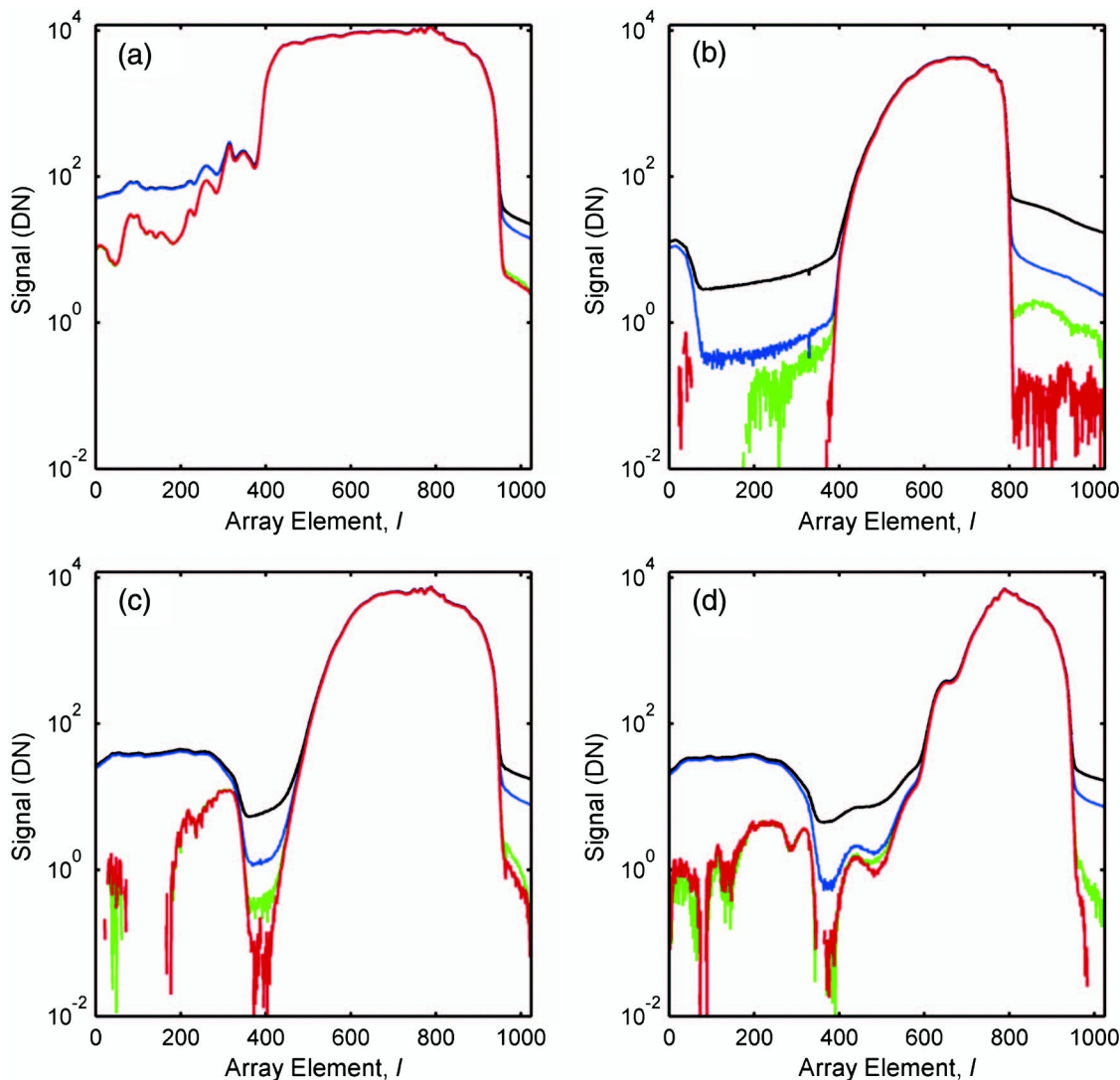


Fig. 10. Validation measurements from (a) channel 1 with an unfiltered Xe lamp; (b) channel 2 with a Xe lamp with a photopic PER filter; (c) channel 3 with a Xe lamp with a BG39 filter; and (d) channel 4 with a Xe lamp with a BG28 filter. Data are shown on a logarithmic scale. The black lines are for all four tracks illuminated, with no SL correction; the blue lines are the signals from the channels when only the single channel is illuminated; the red lines are the SL-corrected signal when the single channel is illuminated; and the green lines are the SL-corrected signals when all channels are illuminated.

entrance pupil. Historically, and in this case, laser-illuminated integrating spheres have been used as the uniform source [1–4].

The lasers were tuned over the spectral range of the system in approximate 50 nm increments, a single channel at a time, and the responses of all detector elements of the instrument were recorded. Figure 4 shows a subset of the laser characterization of the along-track scattering for channel 1. In this system, the transition between properly imaged (IB) and scattered or out-of-band (OOB) radiation was selected to be at 1% of peak value, given by the dark horizontal line in the figure. There was no filtering of higher-order diffracted light from the grating in this system, and second-order scattered blue radiant flux from the grating is imaged in the red spectral region (at twice the wavelength). Figure 5 shows second-order scattering from light in the 450 nm spectral

region imaged onto the detector array in the 900 nm spectral region.

The $D^{\leftrightarrow i,j}$ tensors are partially filled from the laser measurements by first normalizing the scattered light by the IB area of the illuminated channel.

The rest of the $D^{\leftrightarrow i,j}$ elements are filled by interpolating between these laser measurements such that there are values for every element in the arrays.

Figure 6 shows the $D^{\leftrightarrow 3,j}$ tensors that describe scattering within channel 3 and scattering from the other three channels into channel 3. Each tensor has 1024×1024 elements (the number of elements in the detector array). The diagonal tensor, $D^{\leftrightarrow 3,3}$, corresponds to along-track SL; the normalized signal is shown in Fig. 6(c) on a logarithmic scale. Elements along the diagonal, shown as the white line in the

figure, are set to 0. There is a strong feature on the right-hand side of the $\overleftrightarrow{D}^{\leftrightarrow 3,3}$ graph. This feature corresponds to the second-order diffracted light from the grating (Fig. 5). The signals from normalized cross-track coupling matrices, Figs. 6(a), 6(b), and 6(d), are shown on a linear scale. The relatively strong signal from neighboring channels along the diagonal corresponds to light scattered directly opposite the IB signal. The bifurcation in $\overleftrightarrow{D}^{\leftrightarrow 3,4}$, Fig. 6(d), parallel to but offset from the diagonal, is an interesting unexplained artifact of the instrument, likely resulting from a spurious reflection off of an optical surface such as a window or lens.

The 16 $\overleftrightarrow{D}^{\leftrightarrow i,j}$ tensors are combined to form the SDM tensor, \overleftrightarrow{D} , shown in Fig. 7. Within each $\overleftrightarrow{D}^{\leftrightarrow i,j}$ submatrix element, the rows correspond to scattering in channels. So, for example, row 1, which consists of the four

submatrices $\overleftrightarrow{D}^{\leftrightarrow 1,j}$, corresponds to scattering contributions to the signal in channel 1 from channels 1, 2, 3, and 4. The columns correspond to scattering from a channel into the other channels. For example, column 1, the four tensors $\overleftrightarrow{D}^{\leftrightarrow i,1}$, corresponds to scattering from channel 1 into channels 1, 2, 3, and 4. \overleftrightarrow{D} is a square matrix with dimensions equal to the number of channels times the number of detector elements, in this case 4×1024 , or a 4096 by 4096 matrix.

4. Validation Measurements

A simple validation experiment is to illuminate one channel and see if the multichannel correction algorithm properly handles cross-track coupling. Figure 8 shows the results of that test. In this figure, channel 2 was illuminated with a broadband Xe arc source. Uncorrected cross-track coupling is given by the solid

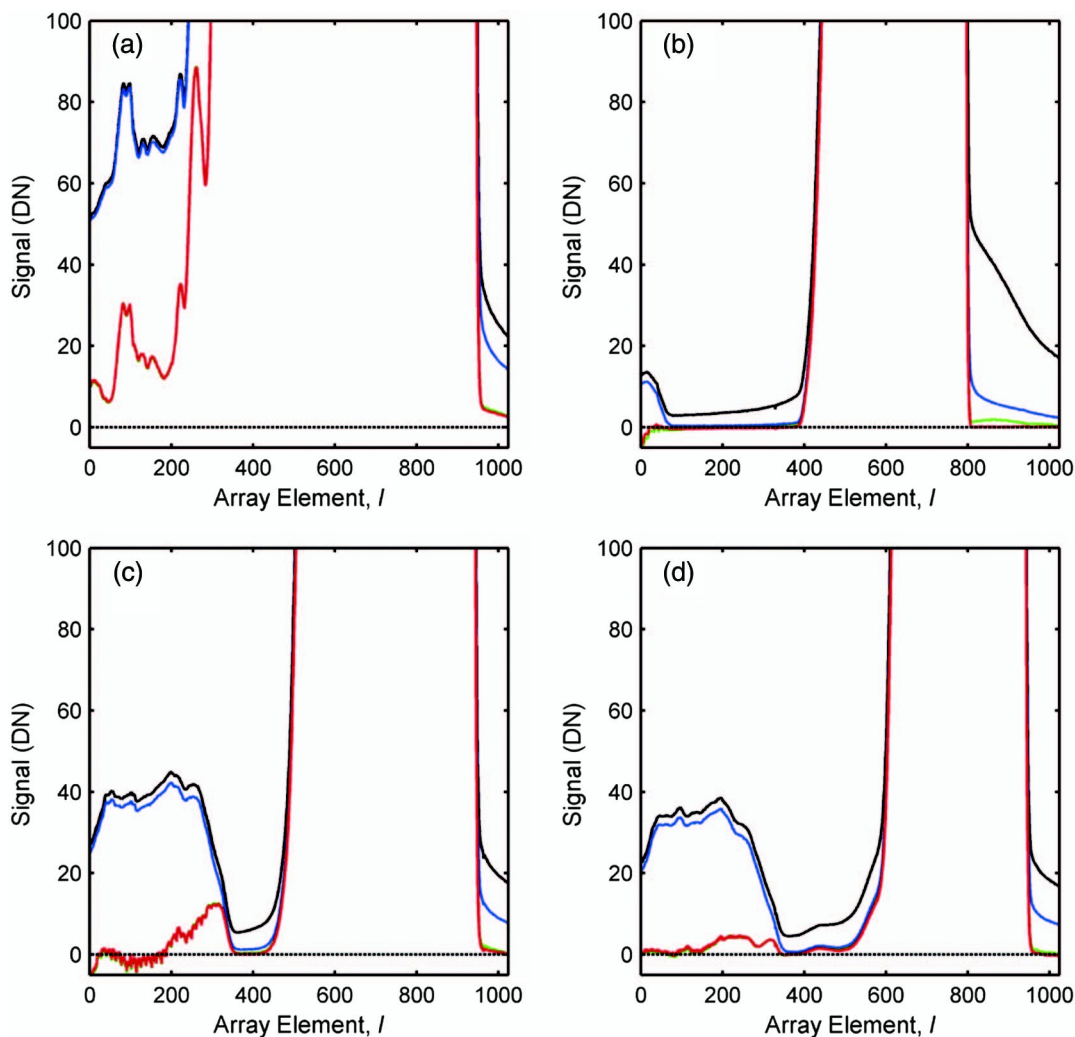


Fig. 11. Expanded view of validation measurements from (a) channel 1 with an unfiltered Xe lamp; (b) channel 2 with a photopic PER filter; (c) channel 3 with a Xe lamp with a BG39 filter; and (d) channel 4 with a Xe lamp with a BG28 filter shown on a linear scale. The black lines are for all 4 tracks illuminated, with no SL correction; the blue lines are the signals from the channels when only the single channel is illuminated; the red lines are the SL-corrected signal when the single channel is illuminated; and the green lines are the SL-corrected signals when all channels are illuminated.

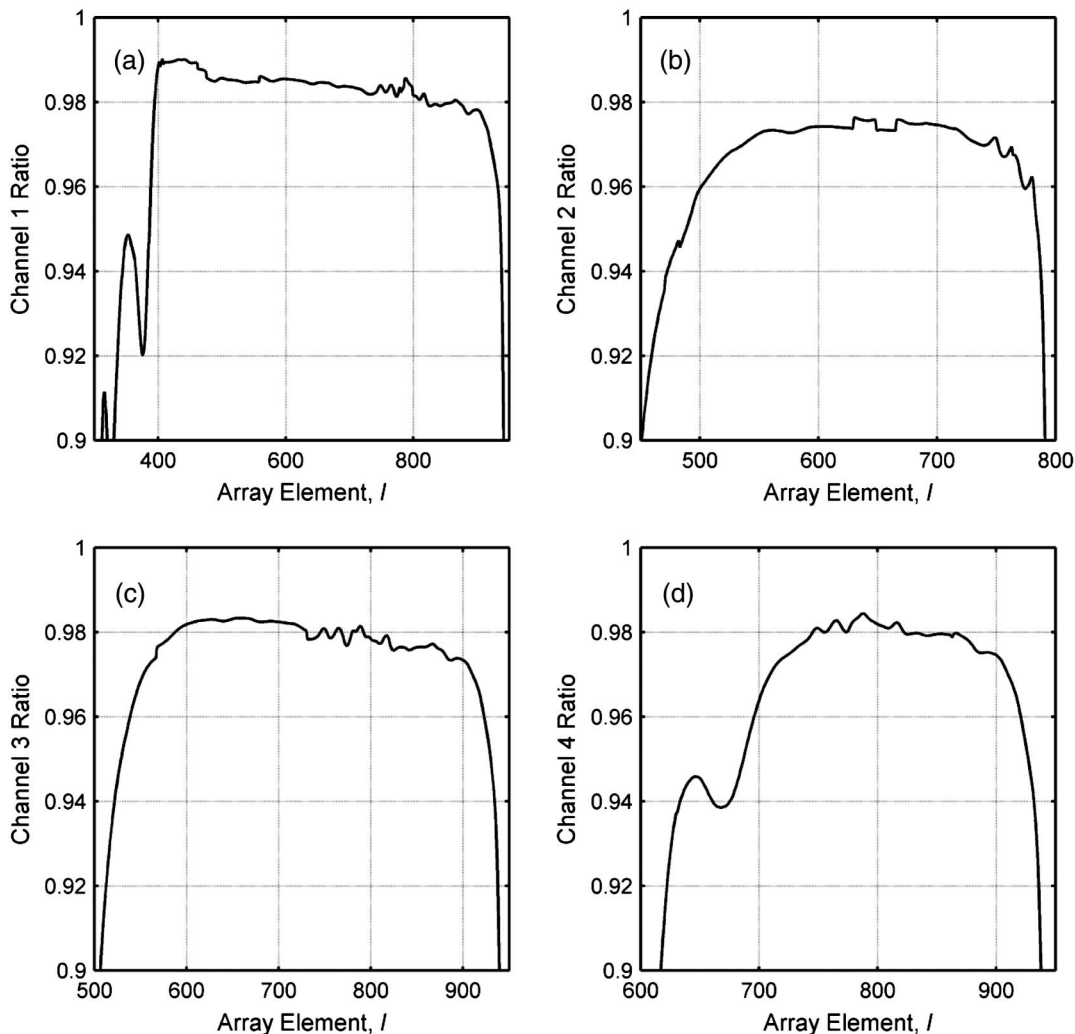


Fig. 12. Ratio of SL-corrected to uncorrected signals from the spectrograph looking at (a) channel with an unfiltered Xe lamp; (b) channel 2 with a photopic PER filter; (c) channel 3 with a Xe lamp with a BG39 filter; and (d) channel 4 with a Xe lamp with a BG28 filter.

colored lines, and SL-corrected cross-track data are given by the dashed colored lines for channels 1, 3, and 4. The SL correction algorithm reduces the magnitude of the cross-track SL signal one to two orders of magnitude, to approximately the 0.1 DN limit.

In a second experiment, a Xe source was used with different-colored filters to validate the efficacy of the multichannel SL correction algorithm. The Xe source was used for one channel, and the Xe source was filtered with an optical glass filter from CVI Laser Corporation simulating the photopic response of the human eye, called a PER filter, and two visible spectrum bandpass Schott glass filters, BG-39 and BG-28, which were used for the other three channels. Filter transmittances are shown in Fig. 9. The filters all have low transmittance in the near IR: the BG-39 and photopic filter transmittances are 0.01% of the peak transmittance or less from approximately 750 nm to 1000 nm. The BG-28 filter has a 0.1% transmittance from 600 nm to 850 nm.

Channel 1 measured the unfiltered Xe source, channel 2 measured the PER filtered Xe source, channel 3

measured the BG-39 filtered Xe source, and channel 4 measured the BG-28 filtered Xe source. Two sets of measurements were made. In the first set of measurements, only one channel was illuminated at a time and the signals from all four channels were measured. In the second set of measurements, all four channels were simultaneously illuminated. The previously developed along-track SL correction algorithm was applied to the single-channel illumination data [1], and the new multichannel correction algorithm was applied to the multichannel data set.

The results are shown in Fig. 10 on a logarithmic scale and in Fig. 11 on a linear scale. The SL correction algorithm for multichannel excitation works as well as the single-channel illuminated SL correction algorithm; in fact, it is difficult to separate the two SL-corrected spectra. The correction reduces the magnitude of the measured signal in spectral regions where there is no incident flux an order of magnitude or greater, with the exception of a region around array element 300 (corresponding to a wavelength of approximately 775 nm). This residual SL signal arises from insufficient characterization of the SL

distribution function in the region where second-order diffracted light impinges on the array (Fig. 5).

The ratios of the corrected signal over the uncorrected signal in regions with measurable signal for the four channels are shown in Fig. 12. The ratio is approximately 0.98 for all four channels and only slightly dependent on the source filter selection. Uncorrected, there is a 2% error arising from SL in the system in the region where the signal is highest for all four channels. The magnitude of the SL-related measurement error is only slightly dependent on the source filter selection. At either end of the array, the SL-corrected to SL-uncorrected ratio is an order of magnitude or greater, increasing as the signal decreases.

5. Future Directions

In the limit where each channel is one pixel wide, the separation between channels is reduced to zero pixels, and there are imaging fore-optics in the system, the algorithm becomes a point-spread correction algorithm applicable to imaging systems with high accuracy requirements in fields ranging from medical imaging to remote sensing. One compelling application is to implement a point-spread correction for the moderate resolution imaging spectroradiometer (MODIS). The finite point-spread response of MODIS impacts both land coverage assessment [14] and ocean color data products [8,9,15]. References [8,9,14,15] have proposed point-spread correction algorithms. Meister *et al.* [9,15] have examined the effects of finite point-spread response (due to SL) on MODIS bands 8 through 16, corresponding to relevant ocean color bands from 412 nm to 869 nm. They showed that the contamination of measured top-of-atmosphere (TOA) radiances due to a large (semi-infinite) cloud is band dependent with measurement errors up to 1.5% at 50 pixels (corresponding to 50 km) from the cloud. They also examined three MODIS Aqua granules and showed that, for the granules they examined, about half of the ocean color pixels are within a 5×7 mask around clouds. Scattered light 10 km from a large cloud ranges from 1% for band 11 (531 nm) to 3% for band 13 (667 nm). These are significant measurement errors compared with the MODIS uncertainty requirements of 2% in reflectance and 5% in radiance [16].

With such large consequences due to SL, it is worthwhile considering a means to validate the correction algorithm and to set uncertainty bounds on the corrected imagery. A means to potentially accomplish that goal is to examine time-series measurements of a well-characterized, radiometrically stable ocean site. Such a site could be in the Southern Ocean where clear ocean measurements have demonstrated stability, or it could be an instrumented site, such as the Marine Optical Buoy (MOBY) site located off the leeward side of Lanai, Hawaii [17], or the Buoy for the acquisition of long-term optical time series (BOUSSOLE) site in the Ligurian Sea off of Nice, France [18].

6. Summary

The SL correction matrix, derived from the SDM, was developed and applied to the correction of a multichannel spectrograph system. Validation measurements of a filtered Xe arc source demonstrate the ability of the correction algorithm to reduce the magnitude of errors arising from SL in the system by one to two orders of magnitude. In addition to providing the first correction of a multichannel spectrograph to SL, it lays the mathematical foundation for a full point-spread response correction for hyperspectral imaging systems.

This work was supported by the National Oceanic and Atmospheric Administration (NOAA) through order number NAO08NES440014 to Moss Landing Marine Laboratories, San Jose State University Research Foundation, and through order number NA10AANEG0253 to NIST's Optical Technology Division. DKC was supported by NIST through order number 70NANB9H9120 to Space Dynamics Laboratory, Logan, Utah, under a joint NIST/Utah State University program in optical sensor calibration.

References

1. Y. Zong, S. W. Brown, B. C. Johnson, K. R. Lykke, and Y. Ohno, "Simple spectral stray light correction method for array spectrometers," *Appl. Opt.* **45**, 1111–1119 (2006).
2. M. E. Feinholz, S. J. Flora, M. A. Yarbrough, K. R. Lykke, S. W. Brown, B. C. Johnson, and D. K. Clark, "Stray light correction of the Marine Optical System," *J. Atmos. Ocean. Technol.* **26**, 57–73 (2009).
3. Y. Zong, S. W. Brown, G. Meister, R. A. Barnes, and K. R. Lykke, "Characterization and correction of stray light in optical instruments," *Proc. SPIE* **6744**, 67441L (2007).
4. Y. Zong, S. W. Brown, K. R. Lykke, and Y. Ohno, "Correction of stray light in spectroradiometers and imaging instruments," presented at CIE 26th Session, Beijing, China, 4–11 July 2007.
5. P. A. Jansson and R. P. Breault, "Correction color-measurement error caused by stray light in image scanners," in *The Sixth Color Imaging Conference: Color Science, Systems, and Applications* (Wiley, 1998), pp. 69–73.
6. A. S. Bolton and D. J. Schlegel, "Spectro-perfectionism: an algorithmic framework for photon noise-limited extraction of optical fiber spectroscopy," *Publ. Astron. Soc. Pac.* **122**, 248–257 (2010).
7. C. Huang, J. R. G. Townshend, S. Liang, S. N. V. Kalluri, and R. S. DeFries, "Impact of a sensor's point spread function on land cover characterization: assessment and deconvolution," *Remote Sensing Environ.* **80**, 203–212 (2002).
8. S. Qiu, G. Godden, X. Wang, and B. Guenther, "Satellite-Earth remote sensor scatter effects on Earth scene radiometric accuracy," *Metrologia* **37**, 411–414 (2000).
9. G. Meister and C. R. McClain, "Point-spread function of the ocean color bands of the moderate resolution imaging spectroradiometer on Aqua," *Appl. Opt.* **49**, 6276–6285 (2010).
10. D. Hong and K. J. Voss, "Effects of point-spread response on calibration and radiometric accuracy of CCD camera," *Appl. Opt.* **43**, 665–670 (2004).
11. B. Bitlis, P. A. Jansson, and J. P. Allebach, "Parametric point spread function modelling and reduction of stray light effects in digital still cameras," *Proc. SPIE* **6498**, 64980V (2007).
12. P. A. Jansson, ed., *Deconvolution of Images and Spectra* (Academic, 1997).
13. S. W. Brown, G. P. Eppeldauer, and K. R. Lykke, "Facility for spectral irradiance and radiance responsivity using uniform sources," *Appl. Opt.* **45**, 8218–8237 (2006).
14. C. Huang, J. Townshend, S. Liang, S. Kalluri, and R. DeFries, "Impact of sensor's point spread function on land cover

- characterization: assessment and deconvolution,” *Remote Sens. Environ.* **80**, 203–212 (2002).
15. G. Meister, Y. Zong, and C. R. McClain, “Derivation of the MODIS Aqua point-spread function for ocean color bands,” *Proc. SPIE* **7081**, 70811F (2008).
 16. J. A. Esposito, A. Wu, and J. Sun, “MODIS reflective solar bands uncertainty analysis,” *Proc. SPIE* **5542**, 448–458 (2004).
 17. “MOBY @ MLML,” <http://moby.mlml.calstate.edu/>.
 18. “BOUSSOLE,” <http://www.obs-vlfr.fr/Boussole/html/home/home.php>.